Correspondence to:
W. Li and K. Zhang,
liwang@cumt.edu.cn;
profkzhang@cumt.edu.cn

Application of a Multi-Layer Artificial Neural Network in a 3-D Global Electron Density Model Using the Long-Term Observations of COSMIC, Fengyun-3C, and Digisonde

Wang Li[1,2] , Dongsheng Zhao[1], Changyong He[2,3], Yi Shen[4], Andong Hu[2,5] , and Kefei Zhang[1,2]

[1]School of Environmental Science and Spatial Informatics, China University of Mining and Technology, Xuzhou, China, [2]SPACE Research Center, School of Science, RMIT University, Melbourne, VIC, Australia, [3]IGN, ENSG, Cité Descartes, Champs-sur-Marne, Marne la Vallée, France, [4]Key Laboratory for Synergistic Prevention of Water and Soil Environmental Pollution, Xinyang Normal University, Xinyang, China, [5]Multi-Scale Group, Centrum Wiskunde & Informatica (CWI), Amsterdam, Netherlands

Abstract The ionosphere plays an important role in satellite navigation, radio communication, and space weather prediction. However, it is still a challenging mission to develop a model with high predictability that captures the horizontal-vertical features of ionospheric electrodynamics. In this study, multiple observations during 2005–2019 from space-borne global navigation satellite system (GNSS) radio occultation (RO) systems (COSMIC and FY-3C) and the Digisonde Global Ionosphere Radio Observatory are utilized to develop a completely global ionospheric three-dimensional electron density model based on an artificial neural network, namely ANN-TDD. The correlation coefficients of the predicted profiles all exceed 0.96 for the training, validation and test datasets, and the minimum root-mean-square error of the predicted residuals is 7.8×10^4 el/cm^3. Under quiet space weather, the predicted accuracy of the ANN-TDD is 30%–60% higher than the IRI-2016 at the Millstone Hill and Jicamarca incoherent scatter radars. However, the ANN-TDD is less capable of predicting ionospheric dynamic evolution under severe geomagnetic storms compared to the IRI-2016 with the STORM option activated. Additionally, the ANN-TDD successfully reproduces the large-scale horizontal-vertical ionospheric electrodynamic features, including seasonal variation and hemispheric asymmetries. These features agree well with the structure revealed by the RO profiles derived from the FORMOSAT/COSMIC-2 mission. Furthermore, the ANN-TDD successfully captures the prominent regional ionospheric patterns, including the equatorial ionization anomaly, Weddell Sea anomaly and mid-latitude summer nighttime anomaly. The new model is expected to play an important role in the application of GNSS navigation and in the explanation of the physical mechanisms involved.

1. Introduction

The ionosphere is populated with large numbers of electrically charged particles, and the charged particles ionized by the action of extraterrestrial radiation can affect the propagation of radio waves. Therefore, a comprehensive understanding of the physical transportation, photoionization and chemical recombination of charged particles in three dimensions has an important role in the ionospheric delay effect, physical mechanism explanation (He et al., 2020; Jin et al., 2017; Li, Yue, Guo, et al., 2018; Li, Yue, Yang, et al., 2018). Currently, the space-borne and ground-based systems fail to provide information about the ionospheric electron density at any time and for any region; thus, it is essential to develop three-dimensional electron density models for ionospheric applications. Starting in the previous century, scientists have developed some famous physical and empirical models, including the Time-Dependent Ionospheric Model (TDIM), Thermosphere-Ionosphere-Electrodynamics General Circulation Model (TIE-GCM), Thermosphere-Iono-sphere-Mesosphere-Electrodynamics General Circulation Model (TIME-GCM), Coupled Thermospheric Ionospheric Model (CTIM), International Reference Ionosphere (IRI), etc. (Bilitza & Reinisch, 2008; Malt-seva & Glebova, 2020; Richmond et al., 1992; Roble & Ridley, 1994; Roble et al., 1988; Schunk & Walk-er, 1973). These models have an important role in simulating the physical and chemical processes that control the variability of three-dimensional charged particles. Each model has its advantages and deficien-cies. Nevertheless, it is still a remarkably challenging mission to simulate the global electron density with

high accuracy, because the ionospheric complex physical mechanism is controlled by several solar-terrestrial factors, including the solar flux, geomagnetic storms, neutral winds and the electric field (Anderson et al., 1998; Atıcı & Sağır, 2020; Du et al., 2019; Karatay, 2020; Schunk et al., 1975).

Traditional ground-based Digisondes measure zenithal ionospheric information with high frequency, but this technique only profiles the bottom-side ionospheric electron densities. Due to the paucity of ionospheric observations, particularly the observations that could measure the altitude distribution of electron density, it is difficult to achieve uniformly accurate ionospheric imaging in low latitudes and polar regions. With the rapid development of the global navigation satellite system (GNSS) radio occultation (RO) technique, the space-based RO technique provides a key capability to profile the global ionospheric three-dimensional structure. Regular occultation profiles obtained from RO systems are an advantageous data source for improving the simulation performance over the oceans in ionospheric modeling. Now, millions of ionospheric density profiles have been gathered by the Constellation Observing System for Meteorology, Ionosphere and Climate (COSMIC), Gravity Recovery and Climate Experiment (GRACE) and Chinese Feng-Yun 3C (FY-3C) missions. These profiles capture the unprecedented, detailed electron density structure in three dimensions. Therefore, it is believed that the data assimilation of multiple ground-based and space-borne sources is a key issue in future ionospheric modeling.

The artificial neural network (ANN) has proven to be a promising tool in solving complex nonlinear problems by systematic learning mechanisms, and it has been applied to develop numerous kinds of ionospheric models successfully, including the total electron content (TEC), critical frequency of the F2 layer (foF2) and peak electron density (NmF2; Athieno et al., 2017; Hernandez-Pajares et al., 1997; Hu & Zhang, 2018; Li, Zhao, He, et al., 2020; Li, Zhao, Shen, & Zhang, 2020; Maltseva & Glebova, 2020; Mansilla, 2019; Sivavaraprasad et al., 2020; Tulasi Ram et al., 2018). ANN was first applied to develop the foF2 model over the Grahamstown Ionosonde (33°S, 26°E) using data from 1973 to 1983. The root mean square error (RMSE) of the simulated residuals was about 0.95 MHz, and the monthly averaged RMSE value reached 0.48 MHz (Williscroft & Poole, 1996). Subsequently, the ANN technique has been widely utilized to build regional ionospheric models in Japan, Southern Africa, China, the Asia/Pacific sector and the auroral zone. An improved Artificial Neural Network-Based Ionospheric Model (ANNIM) was developed using the combined data from COSMIC, GRACE, CHAMP and the global Ionosondes by Tulasi Ram et al., (2018). The RMSEs of the predicted hmF2 (F2-layer peak height) residuals in 2009 and 2002 were 29 and 25 km, respectively. Compared to the Global Ionospheric Peak Height Model (GIPHM) developed using advanced machine learning techniques optimized by the genetic algorithm (Li, Zhao, He, et al., 2020), the predicted accuracy of the ANNIM was slightly lower than that of the following GIPHM model, which had predicted RMSEs of about 26 and 23 km in the solar moderate and minimum year, respectively. Then, the ANNIM model was extended to a complete global three-dimensional ionospheric model (ANNIM-3D; Gowtam et al., 2019). ANNIM-3D not only successfully reproduced the large-scale ionospheric phenomena but also predicted the ionospheric responses to the disturbed geomagnetic environment as well. Previous studies demonstrate that the ANN technique has a great advantage in developing an ionospheric model dependent on the geographic position and solar-terrestrial environment, and the performances of the ANN model are significantly better than some traditional physical or empirical models. However, the performances of ANN-based models are controlled by the input data source, network structure and algorithm. It is believed that the performance of the ANN model could be improved substantially with the development of a data assimilation method.

This study aims to develop a completely global ionospheric three-dimensional model based on the ANN technique by utilizing the long-term observations from space-borne GNSS RO systems (COSMIC and FY-3C) and the Digisonde Global Ionosphere Radio Observatory (GIRO). The organization of the paper is as follows. The datasets and data quality control method are introduced in Section 2.1, and the ANN methodology including the neural network structure and the model's performances are described in Section 2.2. The validations of ANN model performances compared with incoherent scatter radars for quiet and disturbed space environments are presented in Section 3. The predicted capability of the ANN model in capturing some prominent ionospheric dynamic structures, including the Weddell Sea anomaly and the mid-latitude summer nighttime anomaly (MSNA), are validated in Section 4. Finally, the merits and limitations of this model along with expectations for future improvement are discussed in Section 5.
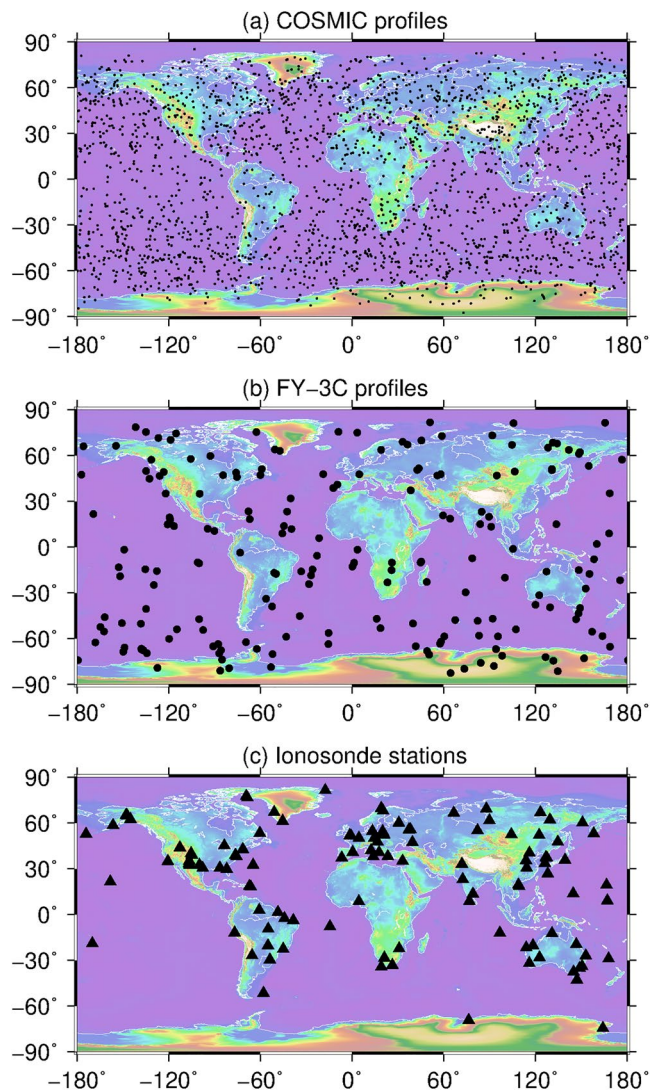
Figure 1. Spatial locations of daily COSMIC, FY-3C profiles and Digisondes of GIRO network. (a) COSMIC, Constellation Observing System for Meteorology, Ionosphere and Climate; (b) FY-3C, Feng-Yun; (c) GIRO, Digisonde Global Ionosphere Radio Observatory.

2. Data and Methodology

2.1. Data and Analysis

In this study, the global distributed ionospheric electron density profiles provided by FORMOSAT-3/COSMIC constellation, FY-3C, and global Digisonde stations are utilized to develop a global ionospheric electron density model. The COSMIC profiles are obtained from the UCAR community programs (https://www.cosmic.ucar.edu/), the FY-3C profiles are downloaded from the National Satellite Meteorological Center (http://satellite.nsmc.org.cn/portalsite/default.aspx) and the Digisonde measurements are downloaded from the Digisonde GIRO (http://spase.info/SMWG/Observatory/GIRO). The periods of three datasets are COSMIC-1 (2007–2016), FY-3C (2014–2019), and Digisonde (2005–2019). The FORMOSAT-3/COSMIC constellation is an international collaborative project between NSPO (National Space Program Office) of Taiwan and UCAR (University Corporation for Atmospheric Research) of the United States of America. This constellation consists of six low-orbit microsatellites was launched on April 15, 2006 (UTC) to collect atmospheric remote sensing data for operational weather prediction, climate, ionospheric (space weather monitoring), and geodesy research. The COSMIC constellation could provide about 2,000–2,500 global distributed electron density profiles when the system was fully operated (http://cdaac-www.cosmic.ucar.edu/cdaac/index.html). The FY-3 series of CMA/NSMC (China Meteorological Administration/National Satellite Meteorological Center) represents the second generation of Chinese polar-orbiting meteorological satellites (follow-on of FY-1 series), and it is operated by the National Satellite Meteorological Center (NSMC) of the China Meteorological Administration. The key aspects of the FY-3 satellite series include collecting atmospheric data for intermediate- and long-term weather forecasting and global climate research (https://directory.eoportal.org/web/eoportal/satellite-missions/content/-/article/fy-3). The first two satellites of the FY-3 series (FY-3A and FY-3B) are considered as research and development missions. Therefore, FY-3C is practically the first operational satellite for the FY-3 series (Liao et al., 2016). The FY-3C spacecraft carried the GNSS Occultation Sounder (GNOS) was launched to an average altitude of 836 km on September 23, 2013, from the Taiyuan Launch Center. Now, this system could observe 150–200 RO events daily. Furthermore, the ground-based observations provided by the GIRO that consists of 120+ global distributed Digisondes are also used. The Digisondes could automatically scale the bottom-side true height electron density profiles, and the scaled profiles are computed by the Automatic Real-Time Ionogram Scaler with true height (ARTIST-5) software (Galkin & Reinisch, 2008). The bottom-side electron density profiles observed by the GIRO network are downloading using the Standard Archive Output (SAO-X, version 3.5.3) Explorer from the Digital Ionogram Data Base (DIDBase) web portal (http://umlcar.uml.edu/DIDBase/). The spatial locations of daily COSMIC, FY-3C RO events, and the Digisondes used in this study are shown in Figure 1.

Sometimes the space-borne and ground-based measurements are affected by instrument failure and severe solar-terrestrial events, therefore the RO profiles and Digisonde observations should be checked for quality control. In this study, for space-borne technique, first the RO profiles are simulated by the Chapman function (Lei et al., 2006), and the correlations between observed profiles and simulated profiles are computed. The RO profiles with the correlations of smaller than 0.85 are removed. Second, some profiles show that the bottom-side electron density values are negative which against the physical regulations, hence these density values are regarded as "noisy" values and removed. For ground-based technique, the quality of Digisonde

data is checked by the upper and lower bounds, which are determined by the mean values ±1.5times standard deviation. The Digisondes only can detect the ionospheric bottom-side electron density profiles but fails to capture the topside ionospheric structure.

Furthermore, the solar-terrestrial environment also controls the variation of ionospheric electron density seriously. For solar activity, the index F10.7 (the noise level generated by the sun at a wavelength of 10.7 cm at the earth's orbit) is used to represent the level of solar radiation. Moreover, high-speed solar wind streams usually have a remarkable impact on the ionospheric electron density, sometimes the sudden ionospheric perturbations can not be attributed to the severe geomagnetic filed motivated by coronal mass ejection or solar flare (Hajra et al., 2017). Therefore, it is believed the index solar wind speed (Vsw) play an important role in improving the performance of the ANN-TDD model. For geomagnetic filed, the indices Dst, Kp, and Ap are used to represent the level of geomagnetic storm. These parameters are obtained from the Space Physics Data Facility of NASA (https://omniweb.gsfc.nasa.gov/).
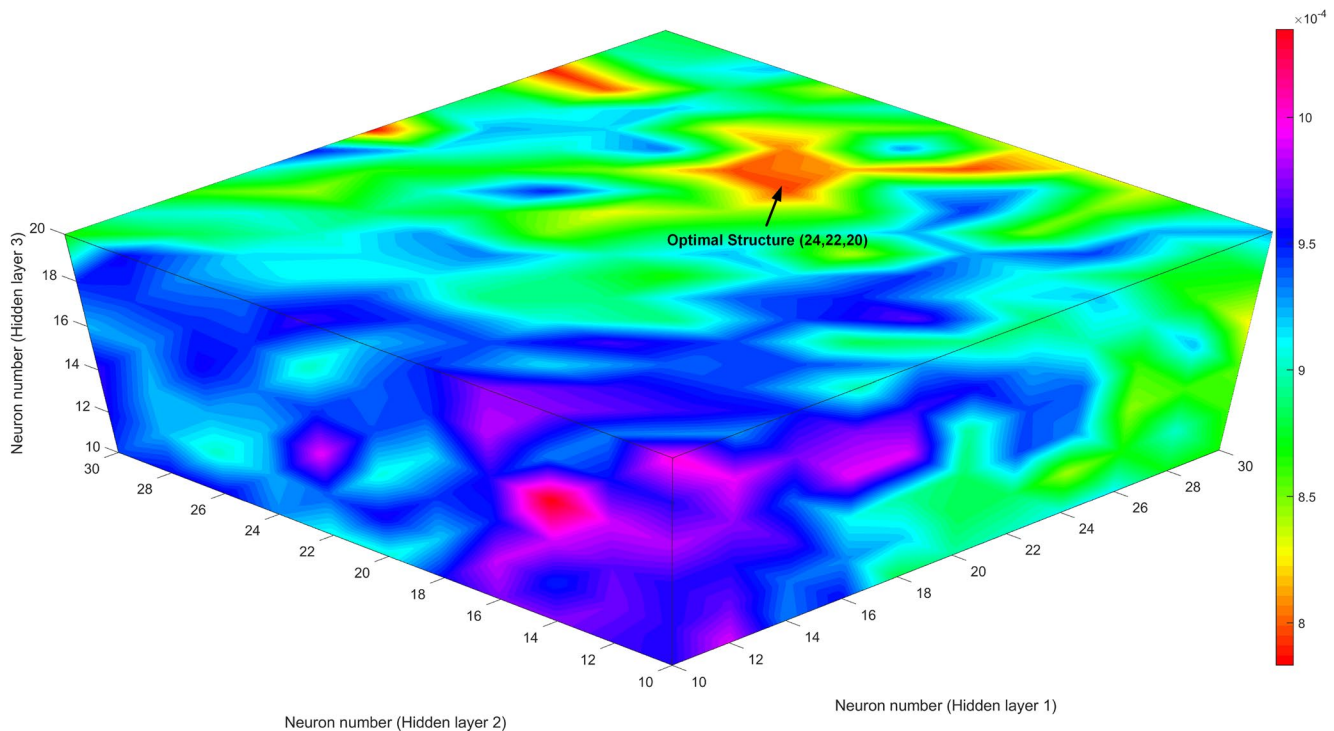
2.2. Artificial Neural Network

Artificial neural network (ANN) has a powerful ability to mimic the human brain to generalize the complicated nonlinear relationship between multiple variables, it has been widely used in the data fitting, clustering, and time series prediction (Haykin, 2007). A traditional neural network contains an input layer, a hidden layer, and output layer, and the layers are connected by neurons. Usually, the output of the preceding neuron is used as the input of the current node via their associated weights, and the output of each neuron in the hidden layers is computed by active functions, such as Tansig, sigmoid, Relu, and Tanh. The numbers of hidden layers and neurons are dependent on the input variables, more details about this relationship the readers could refer to (Gowtam et al., 2019; Tulasi Ram et al., 2018). In the training process, the neural network stops to update the weights and biases when the cost of the validation set increasing for several consecutive steps, in this study the step is set as 6.

In this study, the back propagation (BP) feedforward neural network is used to develop an ionospheric electron density model, namely artificial neural network-based three-dimensional density model (ANN-TDD). During the training process, the entire data set is divided into 10 batches using the mini-batch strategy, and each batch contains about one million vectors. The input parameters include day of year (DOY), local time (LT), geomagnetic latitude (MLAT), geographic longitude (LON), and altitude. Besides, the electron density is also dependent on solar radiation and geomagnetic activity. The parameters F10.7 and Vsw are selected to represent the intensity of solar activity, the parameters Dst, Kp, and Ap are chosen to represent the level of magnetic activity. Furthermore, the numbers of hidden layers and their corresponding neurons are important factors that control the performances of the ANN-TDD model. The BP neural network with three hidden layers are used to develop the ANN-TDD model, and the active functions in three corresponding hidden layers are tansig, tansig, and sigmoid, respectively. Tansig is a neural transfer function, and it calculates a layer's output A from its net input N, the A elements squash into $[-1\ 1]$. This is mathematically equivalent to $A = 2 / \left(1 + \exp\left(-2^{*}N\right)\right) - 1$. The sigmoid activation operation applies the sigmoid function to the input data. This operation is equivalent to $f\left(x\right) = 1 / \left(1 + e^{-x}\right)$. Thousands of experiments are conducted to search the optimal combination of neural neurons in three hidden layers. The result is shown in Figure 2, the root-mean-square error (RMSE) of the ANN-TDD model is minimum when the numbers of neurons are 24, 22, 20 in three hidden layers, the minimum RMSE is about 7.8×10^4 el/cm^3. The detailed structure of the ANN-TDD model is shown in Figure 3.

3. Results

In this study, multiple observations derived from the space-borne COSMIC and FY-3C missions and the ground-based Digisondes are used to develop the ANN-TDD model, and the predicted performances of the ANN-TDD model in the training stage and under various solar-terrestrial environments are analyzed in the following sections.

Figure 2. Statistical RMSEs of the ANN-TDD model with different neurons in three hidden layers. ANN-TDD, artificial neural network-based three-dimensional density; RMSE, root-mean-square error.

3.1. Training Performance

In the training stage, the whole samples are divided into the training set, the validation set and the test set, which contain 70%, 15% and 15% of the samples, respectively. A training data set is a set of examples used to fit the parameters (e.g., the weights of the connections between neurons) during the learning process. Usually, a training data set consists of pairs made up of an input vector and the corresponding output vector. A validation data set is a set of examples used to tune the hyper-parameters of a classifier. The validation datasets can be used for regularization by early stopping, which is helpful to avoid overfitting during the training process. A test data set is independent of the training data set, but it follows the same probability distribution as the training data set. It is only used to evaluate the performance (i.e., generalization) of a fully specified classifier (Provost & Kohavi, 1998). The training results of the ANN-TDD model are shown in Figure 4.

Figure 4 shows the correlations between the measured densities and simulated values of the ANN-TDD model for the training set, validation set, test set and whole sample. The density points in each panel are fitted by the linear function (see the black solid line). The training results show that a majority of points are centered around the solid lines; the correlation coefficients in the four sets are 0.96269, 0.96238, 0.96307, and 0.9627, respectively, and the averaged RMSE is 7.8×10^4 el/cm^3. The correlation coefficients demonstrate that the ANN-TDD model has a strong capability to predict the variation of electron density with high accuracy.

3.2. Predicted Performance in High-Low Solar Activity

Solar radiation is a main energy source for the chemical effect and dynamic transportation of ionospheric electron density. To validate the performances of the ANN-TDD model in the solar maximum year (2015) and solar minimum year (2009), the vertical electron density profiles obtained from the ground-based in-coherent scatter radar (ISR) at Millstone Hill (71.49°W, 42.62°N) and Jicamarca (76.87°W, 11.95°S) are selected as target values. The seasonal validations are shown in Figures 5 and 6; it is noted that each sample
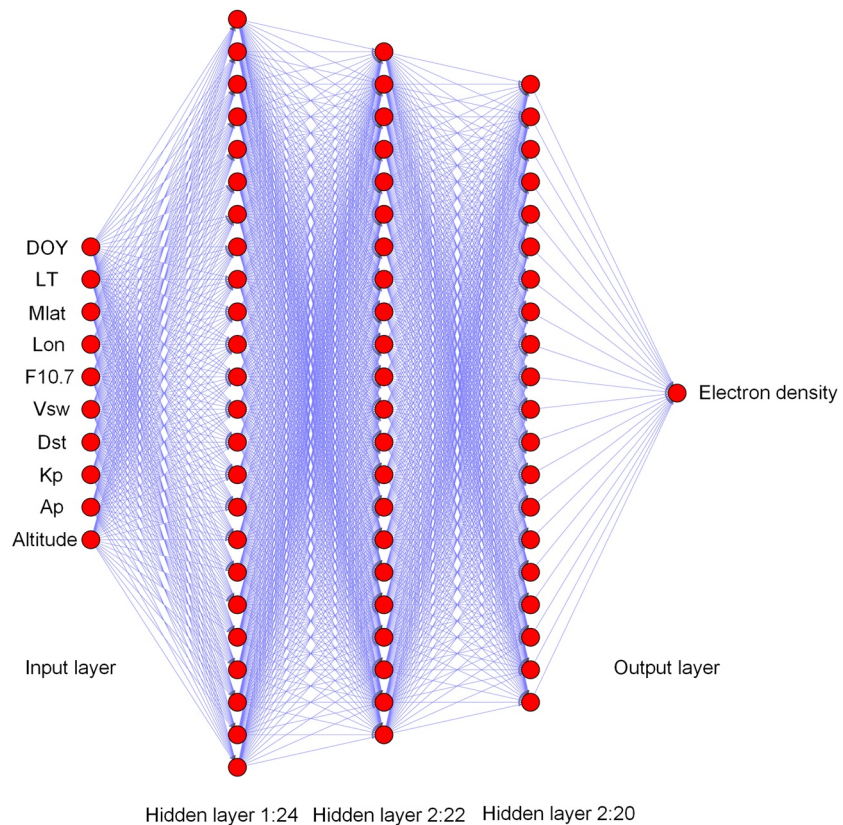
Figure 3. Architecture of the BP feedforward neural network used in the ANN-TDD model. ANN-TDD, artificial neural network-based three-dimensional density; BP, back propagation.

data set contains 5,000 true electron density values. Additionally, the International Reference Ionosphere (IRI-2016) model is also chosen as a comparison object. The comparisons of the performances between the ANN-TDD and IRI-2016 at Millstone Hill and Jicamarca are shown in Figures 5 and 6, respectively.

Figure 5 shows the comparative results of the ANN-TDD and IRI-2016 in spring, summer, autumn and winter during the solar maximum year (2015) and solar minimum year (2009). The correlation coefficients between target profiles and simulations are also computed to evaluate the predicted performances. Generally, the performances of ionospheric models based on the ANN technique are better than those of the IRI-2016 model. For example, in the spring of the solar maximum year (2015), the correlation coefficients of the ANN-TDD and IRI-2016 model are 0.89 and 0.79 and the corresponding RMSEs are 1.01×10^5 el/cm^3 and 1.46×10^5 el/cm^3, respectively (see Figures 5a and 5e). The predicted accuracy of the ANN-TDD model is 30.82% higher than that of the IRI-2016. This phenomenon is also observed in summer, autumn and winter. For example, the predicted RMSEs of the ANN-TDD model in summer, autumn and winter are 9.65×10^4 el/cm^3, 9.07×10^4 el/cm^3, and 1.13×10^5 el/cm^3, and the corresponding RMSEs are 55.94%, 54.42%, and 53.88% smaller than those of IRI-2016. The predicted performances of the ANN-TDD model in summer and autumn are better than those in spring and winter. Compared with IRI-2016, the improved accuracy of the ANN-TDD model exceeds 50% in summer, autumn and winter in 2015.

In the solar minimum year (2009), the comparative results are consistent with those in the solar maximum year. Generally, the predicted RMSEs of the two models in the solar minimum year are lower than those in the solar maximum year. In spring, the RMSEs of the ANN-TDD and IRI-2016 are 6.20×10^4 el/cm^3 and 9.02×10^4 el/cm^3 (see Figures 5i and 5m). Compared with the IRI-2016, the predicted accuracy of the ANN-TDD model is improved by about 31.26%. The performances of the two models in summer, autumn and winter agree well with their performances in spring. For example, as shown from Figures 5j to 5l, the RMSEs of the ANN-TDD model in summer, autumn and winter are 4.89×10^4 el/cm^3, 5.28×10^4 el/cm^3,
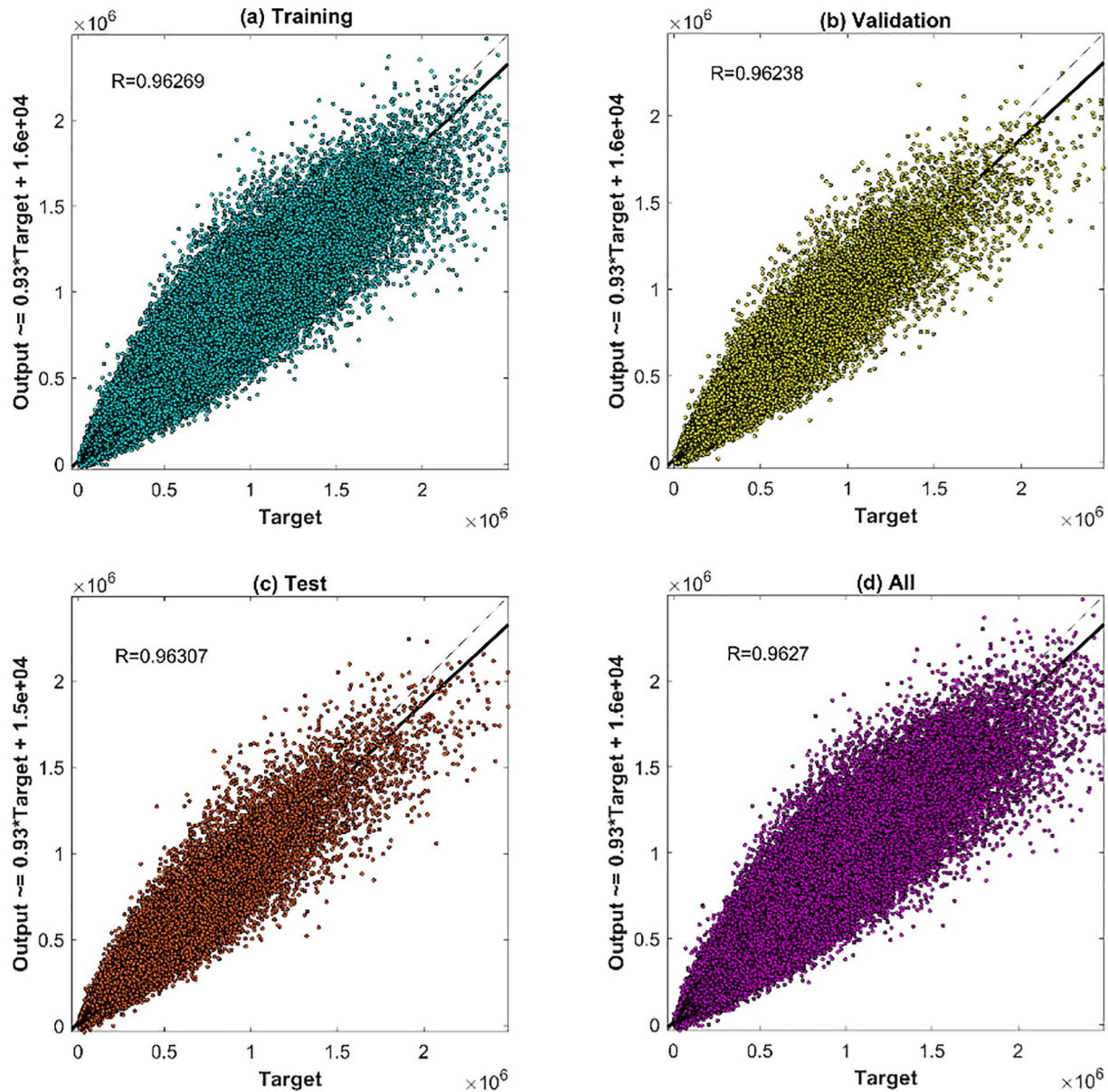
Figure 4. Line regression between the target parameters and simulated values of the ANN-TDD model for the (a) training set, (b) validation set, (c) test set and (d) whole data set. ANN-TDD, artificial neural network-based three-dimensional density.

and 5.52×10^4 el/cm^3, and the corresponding RMSEs are 60%, 52.86%, and 36.27% smaller than those of the IRI-2016. The comparative results demonstrate that for low solar activity, the predicted performance of the ANN-TDD model is also remarkably better than that of the IRI-2016, by 30%–60%.

Similar to the comparative results concerning the Millstone Hill ISR, the predicted performances between the ANN-TDD and IRI-2016 for the Jicamarca ISR are also evaluated, and the comparative results in the solar maximum year and solar minimum year are shown in Figure 6. In the equatorial region, the predicted performances of the ANN-TDD model are also better than those of the IRI-2016 model, which is consistent with the comparative results over the middle-latitude Millstone Hill station. From Figures 6a–6d, the predicted RMSEs of the ANN-TDD in spring, summer, autumn and winter are 1.71×10^5, 1.52×10^5, 1.69×10^5, and 1.94×10^5 el/cm^3, and the corresponding RMSEs are 23.0%, 53.1%, 43.3%, and 46.3% smaller than those of the IRI-2016. The comparative results demonstrate that the ANN technique also improves the accuracy in predicting equatorial ionospheric density by an amplitude of 20%–50% compared to the IRI-2016. This
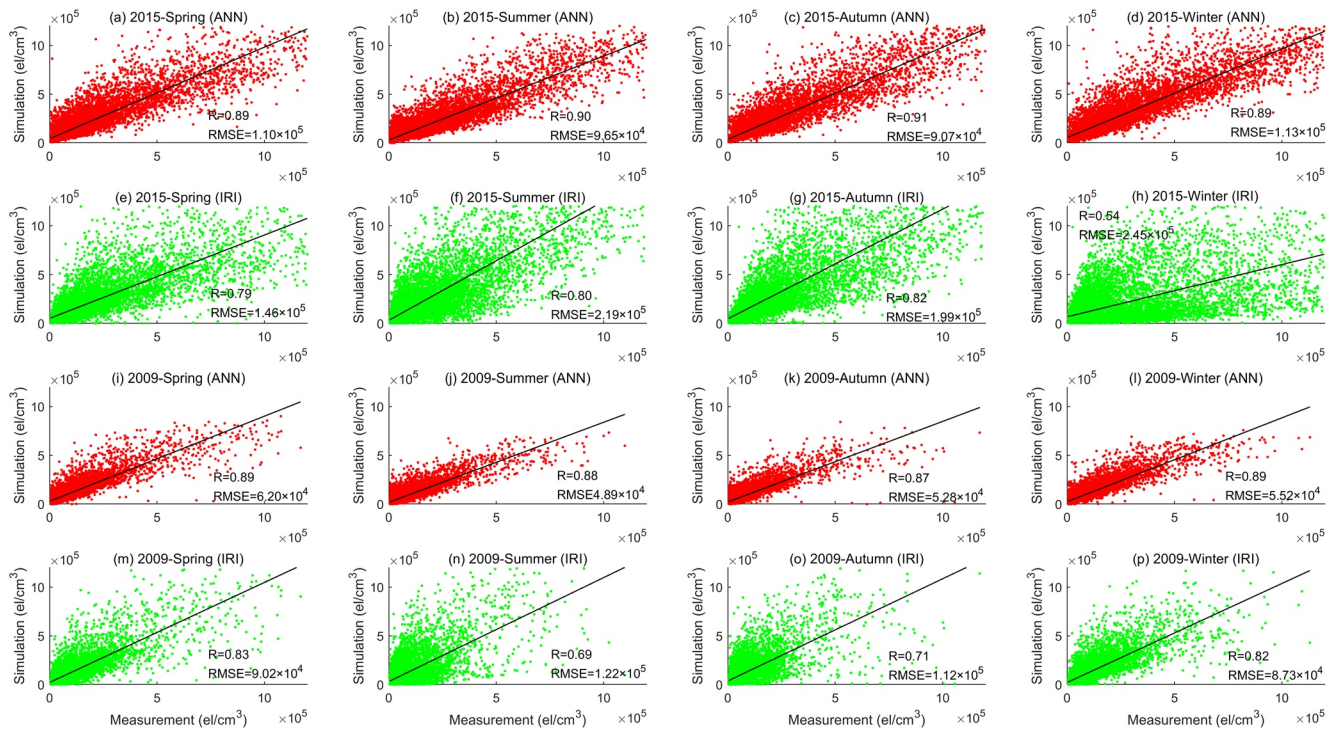
Figure 5. Linear regressions between the Millstone Hill ISR, ANN-TDD and IRI-2016 in the solar maximum year (2015) and solar minimum year (2009). The red and green points signify the predictions of the ANN-TDD and IRI-2016, respectively. ANN-TDD, artificial neural network-based three-dimensional density; IRI, International Reference Ionosphere; ISR, incoherent scatter radar.
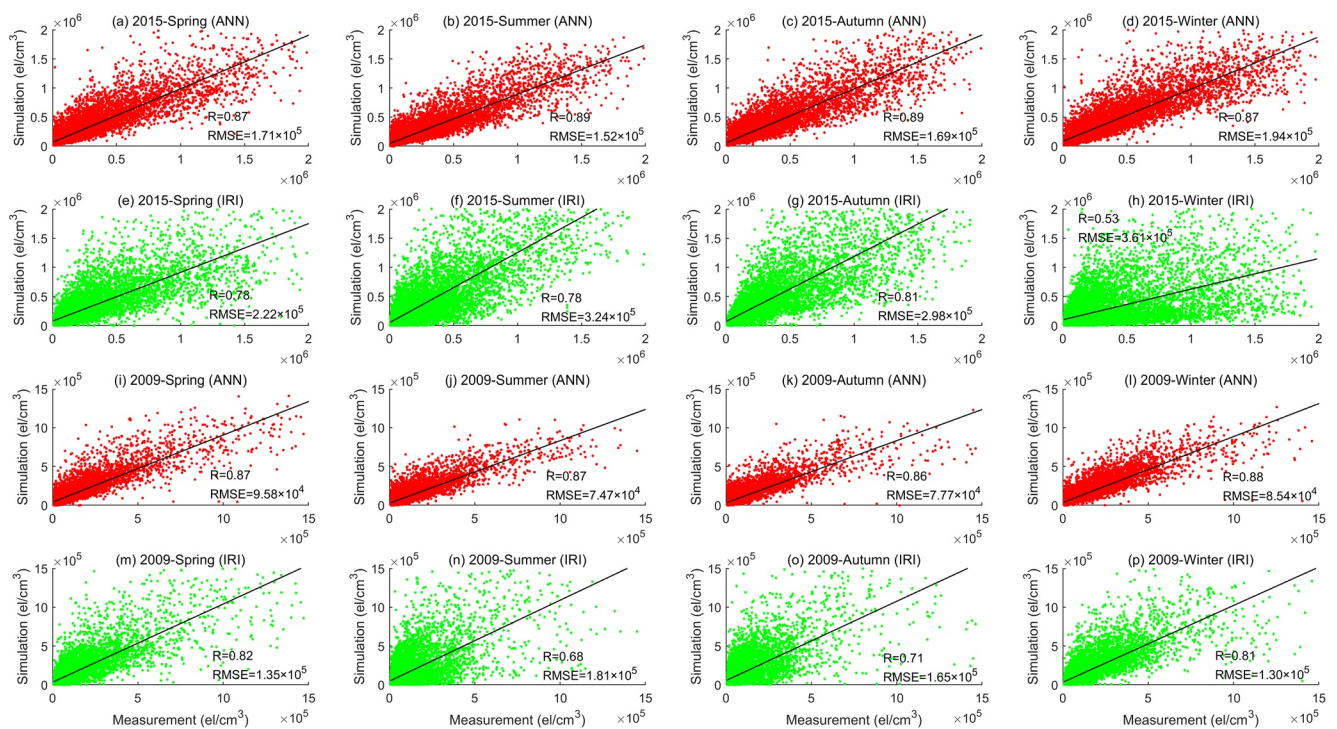
Figure 6. Similar to Figure 5, but for the Jicamarca station.
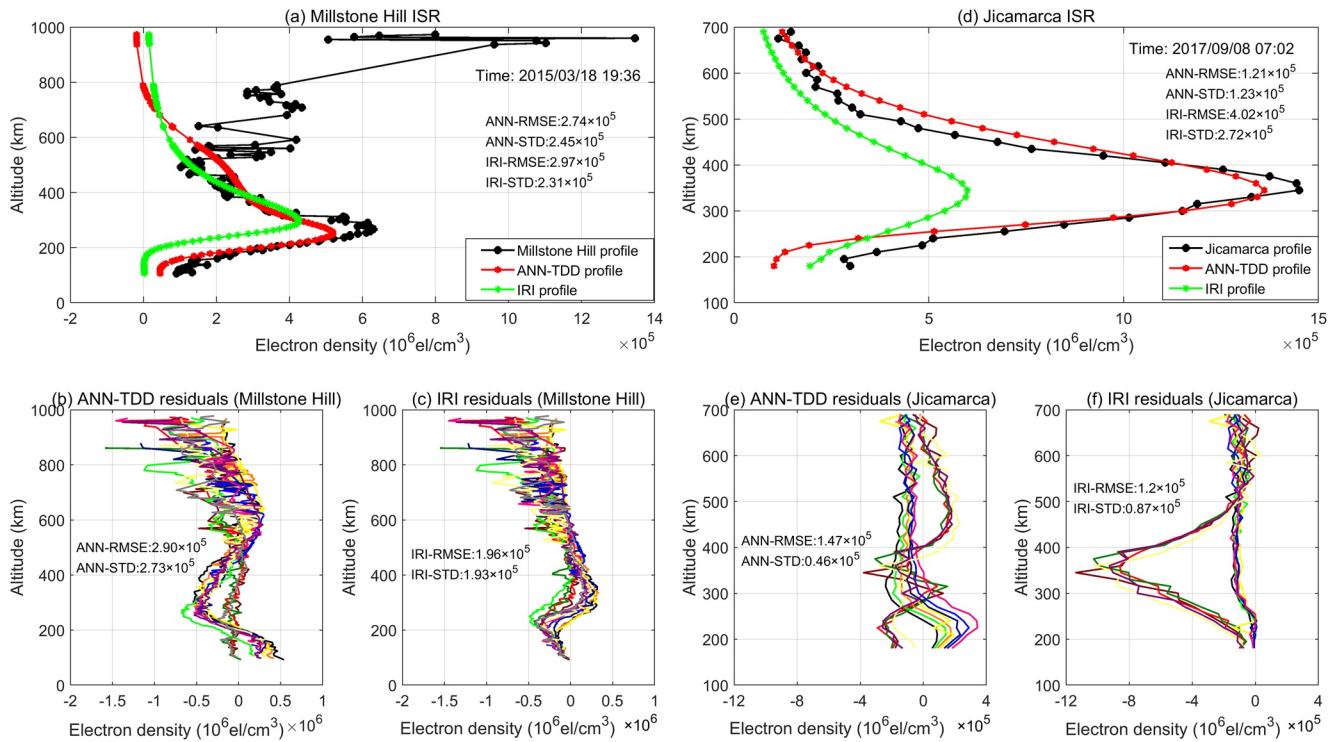
Figure 7. Validations of the predicted profiles of the ANN-TDD and IRI-2016 compared to the electron density profiles derived from the incoherent scatter radars at Millstone Hill and Jicamarca, (a) and (d) represent the comparative results of the ANN-TDD and IRI for example profiles measured by Millstone Hill and Jicamarca ISR, respectively, (b) and (c) represent the predicted residuals of the ANN-TDD and IRI under the March 17–19, 2015 geomagnetic storm at Millstone Hill ISR, and (e) and (f) represent the predicted residuals of the ANN-TDD and IRI under the September 7–9, 2017 geomagnetic storm at Jicamarca ISR. ANN-TDD, artificial neural network-based three-dimensional density; IRI, International Reference Ionosphere; ISR, incoherent scatter radar.

remarkable improvement in modeling equatorial ionospheric electron density is also observed in the solar minimum year. From Figures 6i–6p, the RMSEs of the predicted residuals of the ANN-TDD model are 29%, 58.7%, 52.9%, and 34.3% smaller than those of the IRI-2016.

Figures 5 and 6 indicate that the ionospheric model developed with the ANN technique has a stronger capability in predicting electron density than the IRI-2016 on quiet days in both solar maximum and minimum years. How will the ANN-TDD model perform under severe geomagnetic storms? The authors will further investigate this in the following section.

### 3.3. Predicted Performance Under Severe Geomagnetic Storms

Ionospheric electron density is usually seriously affected by severe geomagnetic conditions (Atıcı & Sağır, 2020; Danilov & Lastovicka, 2001; Fuller-Rowell et al., 1994; Mansilla, 2019). In quiet geomagnetic conditions, the electron density profiles are regular, and their shapes conform to the Chapman function, while in severe conditions, the ionospheric electron densities are greatly disturbed. Predicting high-accuracy electron density is still a great challenge for current ionospheric models. Therefore, it is necessary to evaluate the performance of the ANN-TDD model under severe geomagnetic conditions. In this study, the electron density profiles derived from the Millstone Hill and Jicamarca incoherent scatter radars under the severe geomagnetic storms from March 17 to 19, 2015 and September 7 to 9, 2017 are selected as the reference values, and the predicted profiles of the IRI-2016 model are also computed for comparison. The IRI-2016 has a storm option to investigate the ionospheric dynamic evolution under severe solar-terrestrial conditions specifically, and the availability of the storm model has been validated by many studies in the literature. Therefore, in this paper, the storm option of the IRI-2016 model is turned on. The comparative results of the ANN-TDD and IRI-2016 models during the two geomagnetic storms are shown in Figure 7.

In Figures 7a and 7d, two example electron density profiles observed by Millstone Hill and Jicamarca ISR under severe geomagnetic storms are randomly selected for case studies. From Figure 7a, it is found that the electron density profile is distorted and seriously affected by the violently disturbed geomagnetic field, especially at the topside ionosphere. The predicted profiles of the ANN-TDD and IRI-2016 agree well with the target profile at the bottom-side ionosphere, but neither of them predicts the top-ionosphere electron density enhancement well. The RMSEs of the predicted residuals for the ANN-TDD and IRI are 2.74×10^5 and 2.97×10^5 el/cm^3, and the corresponding standard deviations (STD) are 2.45×10^5 and 2.31×10^5 el/cm^3. For the example profile, the predicted accuracy of the ANN-TDD is much higher than that of the IRI-2016, but the dispersion of the ANN-TDD predicted values is also larger. More details about the predicted capability of the ANN-TDD over the middle latitude region are shown in Figures 7b and 7c. In these figures, about 20 electron density profiles derived from Millstone Hill ISR during the March 17–19, 2015 geomagnetic storm are selected as references. Figures 7b and 7c show that both the profiles of the ANN-TDD and IRI-2016 agree well with the target profiles at the bottom-side ionosphere; the amplitudes of the predicted residuals range from -5×10^5 to 5×10^5 el/cm^3. However, above 600 km altitude, the magnitude of the predicted residuals grows with increasing altitude, and the maximum residual reaches 1.5×10^6 el/cm^3. The RMSEs of the predicted residuals of the ANN-TDD and IRI-2016 are 2.90×10^5 and 1.96×10^5 el/cm^3, and the corresponding STDs for the two models are 2.73×10^5 and 1.93×10^5 el/cm^3. Both the RMSE and STD of the ANN-TDD are larger than those of the IRI-2016 at Millstone Hill ISR. The comparative results indicate that the ANN-TDD has a weaker capability in capturing ionospheric dynamic evolution from a violent, disturbed geomagnetic field at middle latitudes compared to the IRI-2016.

Similar to Figure 7a, the comparative results between the ANN-TDD and IRI-2016 at the near-equator region are shown in Figure 7d. From Figure 7d, an example profile observed by the Jicamarca ISR on September 8, 2017 is selected as a reference. Both of the shapes of predicted profiles of the ANN-TDD and IRI-2016 conform to the Chapman function. The ANN-TDD underestimates the peak density with an amplitude of about 2×10^5 el/cm^3. However, the IRI-2016 negative predicted residuals are more remarkable; the peak density of the IRI-2016 is 2 times smaller than the target profile, with an negative amplitude of about 8×10^5 el/cm^3. Both the RMSE and STD of the ANN-TDD are better than those of the IRI-2016, which indicates that the capability of predicting ionospheric responses to severe space weather of the ANN-TDD may be stronger than that of the IRI-2016 in low latitude regions. To capture more evidence to validate the predicted performances of the two models at the equator, about 15 profiles measured by the Jicamarca ISR from September 7 to 9, 2017 are utilized as targets. The statistical results of the ANN-TDD and IRI-2016 are shown in Figures 7e and 7f. In Figure 7e, the dispersion of the predicted residuals of the ANN-TDD is relatively low, and the absolute magnitude of the residuals is within 4×10^5 el/cm^3 at both the bottom-side and topside ionosphere. However, unlike for the ANN-TDD, the dispersion of the predicted errors of the IRI-2016 is remarkable. For example, several predicted profiles agree very well with the target profiles, with residuals of smaller than 2×10^5 el/cm^3, while other predicted profiles underestimate the peak densities with residuals that exceed 10×10^5 el/cm^3 (similar to Figure 7d). In Figures 7e and 7f, the RMSEs of the predicted residuals of the ANN-TDD and IRI-2016 are 1.47×10^5 and 1.2×10^5 el/cm^3, which indicates that the predicted accuracy of the ANN-TDD is also slightly lower than that of the IRI-2016 at the equator. However, for prediction stability, the ANN-TDD, with an STD of 0.46×10^5 el/cm^3, is significantly superior to the IRI-2016, with an STD of 0.87×10^5 el/cm^3.

3.4. Comparison With FormoSat-7/COSMIC-2 Observations

Sections 3.2 and 3.3 have demonstrated that the ANN-TDD model has a powerful predicted capability under quiet conditions during high-low level solar activities. The ionosphere has well-known global spatial-temporal variations controlled by solar ultraviolet irradiance; therefore, the capability of the ANN-TDD in capturing ionospheric dynamic characteristics must be evaluated. The FormoSat-7/COSMIC-2 constellation is an international collaboration between Taiwan (NSPO) and the United States (NOAA) that uses a constellation of six remote sensing microsatellites to collect atmosphere-ionosphere-thermosphere profiles for weather prediction, climate change and gravity research. The FormoSat-7/COSMIC-2 constellation is a follow-up mission to the FormoSat-3/COSMIC mission to meet RO data continuity requirements, and the six microsatellites include two payloads: a Radio Frequency Beacon (RFB) transmitter and an Ion Velocity Meter (Meter) were launched into low-inclination orbit on June 25, 2019. Now, the six-satellite constellation
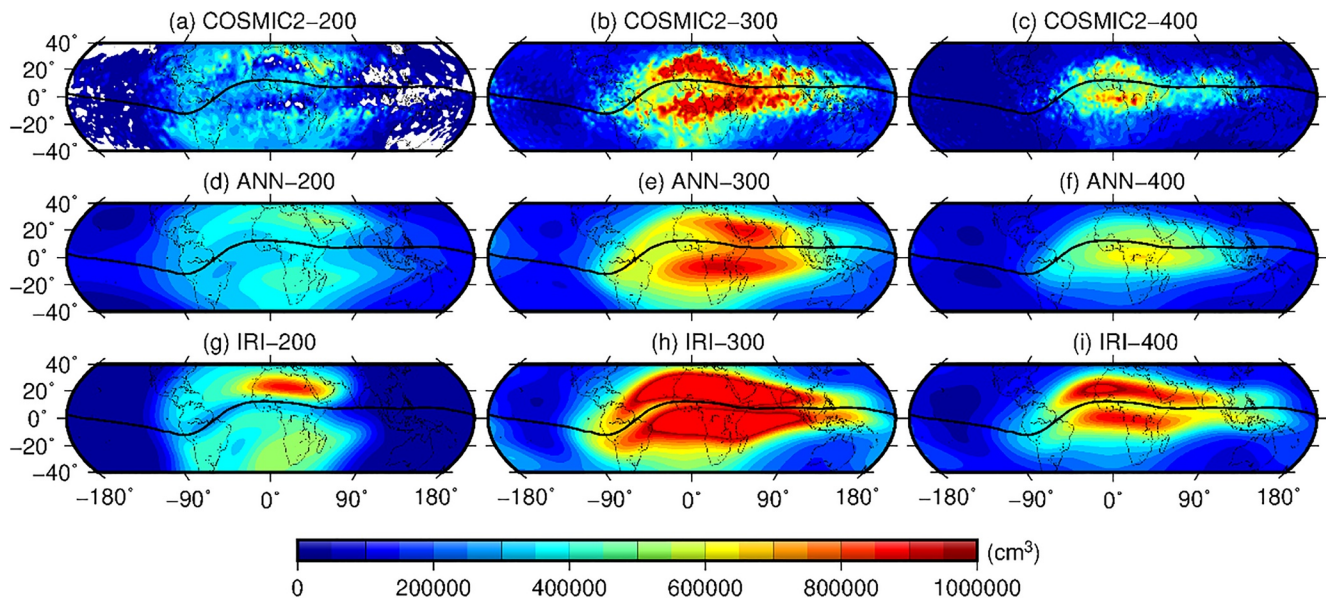
Figure 8. Comparisons of global ionospheric electron density maps produced by the COSMIC-2 profiles, ANN-TDD, and IRI-2016 model spans from 200 to 400 km with an interval of 100 km in March 2020, the black line is the magnetic equator. (d)-(f) ANN-TDD, artificial neural network-based three-dimensional density; (a)-(c) COSMIC, Constellation Observing System for Meteorology, Ionosphere and Climate; IRI, International Reference Ionosphere.

can track more than 4,000 high-quality profiles per day, and the quality of the profiles has been validated by (Tsai et al., 2019). In this study, the COSMIC RO profiles measured in spring and winter are selected to reconstruct the global ionospheric electron density maps within altitudes of 200–400 km. These maps are used as references to evaluate the performances of the ANN-TDD model in capturing global ionospheric spatial-temporal characteristics under different levels of solar activity. The validations are shown in Figures 8 and 9.

In Figure 8, the COSMIC RO profiles from UT11:00–13:00 from March 10 to March 30 in 2020 are utilized to reconstruct global ionospheric electron density maps with a spline interpolation algorithm, as shown in the panels of the top row. During this period, the solar activity is quiet; therefore, the variation of ionospheric electron density is relatively stable. Now, the six FormoSat-7/COSMIC-2 satellites are positioned in a low inclination orbit at a nominal altitude of ~520–550 km with an inclination of 24°, and the geographic coverage of RO profiles of the COSMIC-2 constellation is 40°S ~ 40°N. For more details about the geographic coverage of daily COSMIC-2 RO profiles, the reader can refer to (https://www.cosmic.ucar.edu/what-we-do/cosmic-2/). Therefore, the comparative results of three kinds of products are validated within 40°S~40°N.

From the panels in the top row, the ionospheric electron density values have an obvious relationship with geographic position and altitude. Large values of electron density distribute in the Africa-India sector densely, and two high-amplitude electron density crests are located at low latitudes along the magnetic equator; this is called the equatorial ionization anomaly (EIA; R. Raghavarao, 1988). For altitude, a large number of electrons gather at a height of 300 km with a peak value of 1.0×10^6 el/cm^3; the electron density in this layer is 3–4 times larger than that in the neighboring layers of 200 and 400 km. The simulated maps of the ANN-TDD model in the middle row agree well with the COSMIC-2's products. The ANN-TDD model not only successfully captured the EIA feature, but also has a powerful high-accuracy prediction ability. In general, the ANN-TDD model tends to underestimate the electron density, and this conforms to the comparative results in Figure 7. For example, in Figure 8e, the maximum value of electron density predicted by the ANN-TDD is 8.5×10^5 el/cm^3, which is lower than the reference by 15%. Like the ANN-TDD, the IRI-2016 model can also simulate the global ionospheric spatial-temporal characteristics well, but this model tends to overestimate the electron density. For example, in Figure 8h, the scope of high-amplitude electron density predicted by the IRI-2016 model covers South America and the Africa-India-Southeast Asia sector; this is much larger than the reference. Besides, the maximum value predicted by the IRI-2016 is higher than the reference by more than 30%. This phenomenon is also observed in Figure 8i.
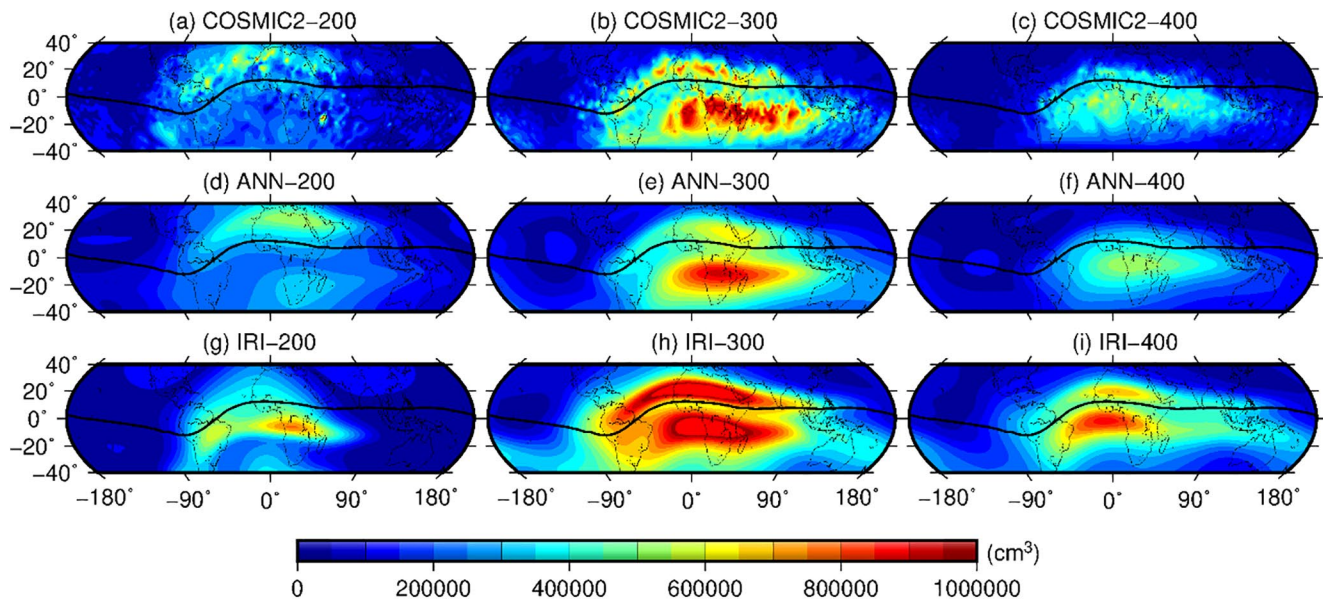
Figure 9. Similar to Figure 8, but in December 2019. (a)-(c) COSMIC, Constellation Observing System for Meteorology, Ionosphere and Climate; (d)-(f) ANN-TDD, artificial neural network-based three-dimensional density; (g)-(i) IRI, International Reference Ionosphere.

The COSMIC RO profiles in the period of UT11:00–13:00 from December 10–December 30, 2019 are utilized to reconstruct global ionospheric electron density maps in winter for the northern hemisphere, as shown in the panels of the top row in Figure 9. Both of the predicted maps of the ANN-TDD and IRI-2016 agree with the COSMIC-2 products, and all three kinds of winter maps (for the northern hemisphere) could capture the EIA characteristics. However, unlike the EIA features in spring, the EIA in winter has a special structure dependent on altitude. For example, at the altitude of 200 km (Figure 9a), the north crest of EIA-covered North Africa is much stronger than the south crest, and the maximum value (about 4×10^5 el/cm^3) of the north crest is 2–3 times larger than the south crest. However, at the altitude of 300 km, the south crest of the EIA grows stronger remarkably and covers southern Africa and the Indian Ocean, with a maximum value of 9×10^5 el/cm^3, while the scope and magnitude of the north crest weaken significantly. At the 400 km layer, the two crests move closer to the magnetic equator, and the EIA pattern cannot be observed in this layer. From the panels in the middle row, the three-dimensional EIA structure simulated by the ANN-TDD model agrees well with the COSMIC-2 products, and the ANN-TDD model underestimates the electron density by 10%–15%. This is consistent with the results in Figure 8. However, the EIA structures simulated by the IRI-2016 within the altitudes of 200–400 km are contrary to the reference maps (see Figures 9g–9i), and the IRI-2016 overestimates the density by more than 30%, especially at the 300 km layer.

Many studies reported that the EIA is controlled by the equatorial plasma fountain effect: the equatorial upward $E \times B$ drift lifts the plasma from the magnetic equator to high altitudes, and the accumulated plasmas diffuse down to high latitudes along the geomagnetic field lines. The diffusion process results in the two ionization crests on both sides of the magnetic equator (Balan & Bailey, 1995; Lin, Wenbin, et al., 2007). In the drift and diffusion processes, the strength of the fountain effect and thermospheric neutral winds control the EIA formation significantly. On the one hand, a stronger plasma fountain drifts more plasmas to higher altitudes, which creates stronger and more poleward extended crests of the EIA. On the other hand, a stronger thermospheric equatorial neutral wind could sustain the plasma at higher altitudes for a longer time, which contributes to enhancing the strength of EIA crests. These factors explain why the crests in the lower latitudes are more poleward.

The strength of the equatorial fountain effect controls the development of the EIA, and the thermospheric neutral winds alter the symmetrical structure of the EIA through field-aligned plasma transport (Tulasi Ram et al., 2009). In the summer hemisphere, the summer-to-winter neutral winds will drive the plasmas in the equatorward/upward direction, but the equatorial fountain process diffuses the plasma in the

poleward/downward direction. The downward diffusion direction driven by the equatorial fountain process is same as the direction produced by the thermospheric neutral winds. Therefore, the asymmetrical structure of the EIA is determined by the relative contributions from the equatorial fountain process and thermospheric neutral winds. For example, in Figure 9, the trans-equatorial neutral winds are dominant in the morning, and they drive the plasmas from the summer hemisphere to the winter hemisphere along the magnetic field line, which causes the north crest in the winter hemisphere to be stronger than the south crest during the morning hours. However, the equatorial fountain process reaches its maximum strength at noon; this process is dominant over the thermospheric neutral winds and weakens the magnitude of summer-to-winter plasma transportation. Hence, interhemispheric transportation of plasma driven by neutral winds is minimized in the afternoon; this is the reason that the south crest in the summer hemisphere is stronger than the north crest at noon, which is consistent with the asymmetry of the EIA in Figure 9.

3.5. Prominent Regional Ionospheric Anomalies

Sections 3.2–3.4 have demonstrated that the ANN-TDD model has a powerful ability to predict global high-accuracy electron density under high-low level solar activities. Usually, solar radiation is the main energy source for the ionization and combination processes of the ionosphere, but ionospheric convection is also controlled by other factors, including the eastern electrical field, neutral winds, particle precipitation, etc. These driving forces also contribute to some prominent regional ionospheric patterns, such as the EIA, Weddell Sea anomaly, Mid-latitude summer nighttime anomaly and winter anomaly. It is believed that a perfect ionospheric model should not only have a strong capability to predict high-accuracy ionization processes but should also successfully capture the global or regional ionospheric dynamic features, including diurnal and seasonal variation, the EIA, the Weddell Sea anomaly, etc. Therefore, two prominent regional ionospheric patterns are simulated to validate the ANN-TDD's capability in capturing large-scale ionospheric dynamic characteristics.

3.5.1. Weddell Sea Anomaly

The Weddell Sea anomaly is characterized by fact that the plasma density over the Weddell Sea at night is larger than during the day. The phenomenon can be observed in the spring, autumn and winter. This anomaly was first detected by the Falkland Ionosonde (60°W, 52°S) near the Weddell Sea in 1957 (Bellchambers & Piggott, 1958). In this study, the ANN-TDD model simulates the hourly global electron density maps and the vertical structure of the Weddell Sea anomaly on December 22, 2013, and the results are shown in Figure 10.

The left panels in Figure 10 show the hourly variations of global electron density maps from LT19:00, December 22, 2013, to LT06:00, December 23, 2013; it should be noted that the time system is in local time (LT). In December, the southern hemisphere is the summer hemisphere, and the electron density in the summer hemisphere is much higher than that in the winter hemisphere because of the stronger photoionization effect, as shown in Figures 10a and 10b. In the daytime, the value of the electron density is inversely proportional to the latitude. Large numbers of electrons gather around the magnetic equator, with a maximum value of 1×10^6 el/cm³, which is about 5 times larger than that in the polar regions. After sunset, the electron density around the magnetic equator depletes, while the electron density over the Weddell Sea enhances from LT20:00. At midnight, the electron density over the Weddell Sea reaches a peak value of 6.5×10^5 el/cm³. After that, the Weddell Sea enhancement gradually weakens and disappears at dawn. In brief, the duration of the Weddell Sea anomaly phenomenon is about 10 hours, and its magnitude is 2–3 times larger than the daytime value.

Figure 10m shows the vertical structure of the Weddell Sea anomaly at the layers spanning from 200 to 450 km with an interval of 50 km on the winter solstice, 2013. The structure of the Weddell Sea anomaly is consistent with the EIA. The Weddell Sea nighttime enhancement appears starting in the 250 km layer and reaches a peak value of 8×10^5 el/cm³ at the 350 km layer. Besides, the nighttime enhanced densities aren't limited to appearing over the Weddell Sea; the phenomenon covers the scope of 120°W–30°W, 60°S–90°S, which is consistent with the observational map of TOPEX/Poseidon radar altimeter (Horvath, 2006). The results in Figure 10 demonstrate that the ANN-TDD model successfully captures this ionospheric dynamic feature over the aurora zone.
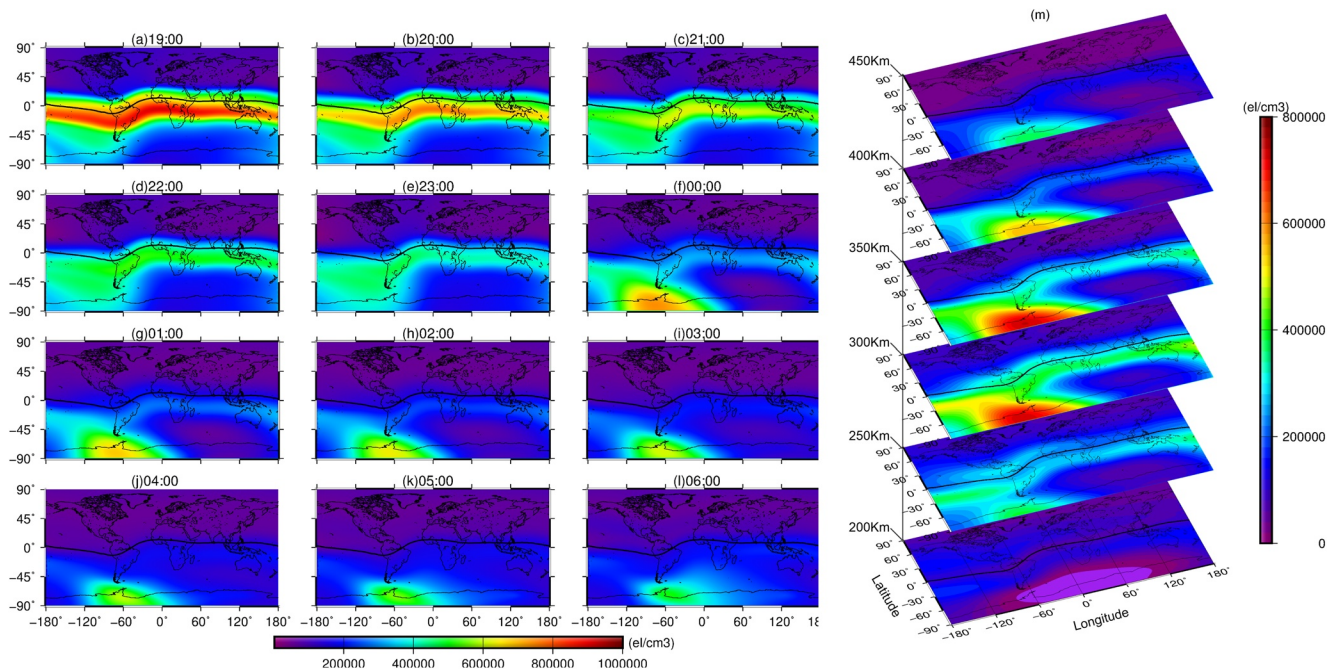
Figure 10. Horizontal-vertical structures of Weddell Sea anomaly on December 22, 2013, (a)-(l) show the hourly variations of global electron density maps at the altitude of 300 km layer, (m) shows the vertical structures of Weddell Sea anomaly at the layers span from 200 to 450 km with an interval of 50 km.

The eastward magnetic declination at the Weddell Sea and the southward offset of the magnetic equator are supposed to be major reasons for the enhanced electron density after sunset (C-H Lin et al., 2009). The geomagnetic pole is seriously offset from the geographic pole in Antarctica, which causes the longitudinal asymmetry of the geomagnetic field in the southern hemisphere. In the 30°–120°W longitudinal sector, the geographic latitude is higher than the geomagnetic latitude in the middle latitudes of the southern hemisphere. For example, the geographic latitude of the Weddell Sea is 68°S, while the corresponding geomagnetic latitude is 60°S. Therefore, the southward offset of the magnetic equator makes the southern crest of the EIA move to the Weddell Sea. Besides, the eastward wind, affected by eastward magnetic declination, will generate a northward/equatorward component along the geomagnetic field line, and the strong equatorward wind can uplift the ionospheric layers to a higher altitude. The magnetic declination in the corresponding region of the Weddell Sea in the eastern hemisphere is much smaller than the angle in the Weddell Sea; thus, the equatorward wind in this region need not be considered. In addition to the southward excursion of the magnetic equator and the uplifted process caused by the equatorward wind, both the plasma diffused downward from the topside ionosphere in the nighttime and the photoionization at the Weddell Sea provide fresh plasma to enhance the anomaly (Burns et al., 2008). It is noted that particle precipitation and photoionization also occur in the eastern hemisphere, but the larger inclination angle and weaker equatorward wind in this region make the fresh plasma diffuse to lower altitude quickly, which results in less plasma accumulation. Therefore, the nighttime enhanced anomaly is not observed in other longitudinal sectors, except the Weddell Sea.

3.5.2. Mid-latitude Summer Nighttime Anomaly

The mid-latitude summer nighttime anomaly (MSNA) is characterized by the fact that the nighttime electron density is larger than it is in the daytime over the middle latitudes of the summer hemisphere. In the southern hemisphere, the MSNA is called the Weddell Sea anomaly; the phenomenon was first observed in the 1950s. With the development of the GNSS RO technique, the nighttime enhanced plasma was also observed in the middle latitudes of the northern hemisphere. In this study, the horizontal and vertical electron density variations on June 22, 2019 are simulated by the ANN-TDD to evaluate the model's performance over middle latitudes in the northern hemisphere. The results are shown in Figure 11.
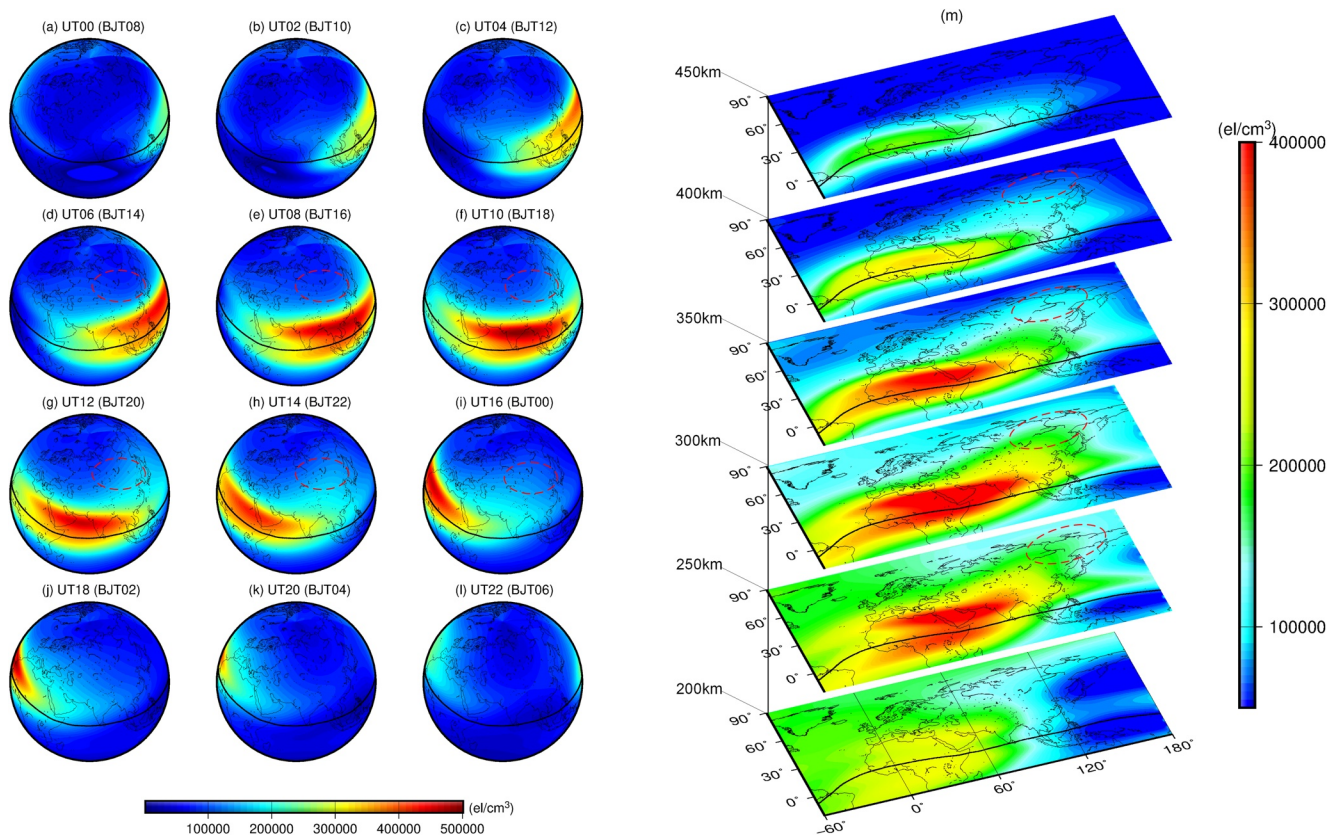
Figure 11. Horizontal-vertical electron density distribution on June 22, 2019. (a)-(l) show the hourly variation of global ionospheric electron density in universal time (UT) and Beijing time (BJT), BJT = UT+8. (m) shows the electron density at the layers span from 200 to 450 km with an interval of 50 km, the black line is the magnetic equator.

Previous studies in the literature reported that the nighttime enhanced electron densities usually appear over the regions of Central-East Asia and Siberia (Thampi et al., 2009; Xiong & Lühr, 2014). In Figure 11, the regions of Central-East Asia and Siberia are marked by red circles. The panels in the left column of Figure 11 show the hourly variations of electron density over Europe and Asia on the summer solstice, 2019, during the period of UT04 to UT10 (for BJT, the local time is 12–18). The interesting area is located in the sunlit hemisphere, and the averaged amplitude of electron density is about 1.4×10^5 el/cm³. After BJT18:00 (Figure 11f), the regions in red circles move into the dusk sector, while the magnitude of the electron density gradually increases and reaches a maximum value of 1.9×10^5 el/cm³ at BJT22 (UT14).

The panels in the right column of Figure 11 show the vertical structure of the MSNA in the layers spanning from 200 to 450 km with an interval of 50 km at BJT22 (UT14). It is found that the electron density is inversely proportional to the geomagnetic latitude, and the magnitude of the electron density over the equator is 2–3 times higher than that over the Polar Regions. At BJT22, the subsolar region is the North Africa-India sector, and high-concentration electron densities gather at the sections of North Africa and India; the maximum amplitude exceeds 4×10^5 el/cm³. At the 200 km layer, the electron densities in the middle latitudes of the nighttime hemisphere, including Central-East Asia and Siberia, are smaller than that in the same latitudes (e.g., Europe) of the sunlit hemisphere. However, above 250 km altitude, a significant poleward electron density enhancement appears in the middle latitudes of the nighttime sector, as shown in the red circles. For example, the nighttime electron densities (UT14, 22 for BJT) over northeast Asia and Siberia are higher than the daytime electron densities (UT14) over Europe within the altitudes of 250–400 km. The nighttime poleward electron density enhancement is most prominent at an altitude of 300 km. In this layer, the averaged electron density in the red circle is about 2×10^5 el/cm³, which is 0.8×10^5 el/cm³ larger than that over Europe. Above 450 km, the MSNA phenomenon cannot be observed. The results are consistent

with these works (Chen et al., 2012; C-H Lin et al., 2010). Figure 11 demonstrates that the ANN-TDD model has a powerful capability in capturing ionospheric dynamic features in middle latitudes.

The physical mechanism of the MSNA is similar to the Weddell Sea anomaly: the northern crest of the EIA moves poleward to higher latitudes controlled by the E × B drift. Because of the later sunset time, the fresh plasmas ionized by the additional photoionization diffuse to the northward crest, which creates a new electron density crest in the 30°–60°N latitudinal zone. Besides, the equatorward wind in the middle latitudes of the northern hemisphere could uplift the ionospheric layer to a higher altitude, which slows down the recombination of ions and electrons and reduces the particle loss rate.

4. Discussion and Conclusion

This study is a further extension of the ANN algorithm proposed by Li, Zhao, He, et al., (2020). Based on the success of the ANN model in predicting ionospheric peak parameters foF2 and hmF2, this study uses the profiles obtained from multiple RO systems (COSMIC-1, FY-3C) and the observations of global Digisondes to develop a completely global three-dimensional electron density model with an artificial neural network, namely ANN-TDD. In the training stage, the correlation coefficients of the datasets all exceed 0.96 in training, validation and test sections, and the RMSE of the predicted residuals of the ANN-TDD is 7.8×10^4 el/cm^3, which reveals that the ANN-TDD model has perfect performance in learning ionospheric nonlinear characteristics and a strong capability in predicting the electron density with high accuracy. The predicted capability of the ANN-TDD is thoroughly validated with the profiles derived from the Millstone Hill and Jicamarca ISR under high-low level solar activities and severe geomagnetic storms, alongside the well-established empirical model IRI-2016. The comparative results indicate that the predicted densities of the ANN-TDD are consistent with the profiles measured by the Millstone Hill ISR at middle latitudes. The minimum RMSEs of the ANN-TDD model in the solar maximum year and solar minimum year are 9.65×10^4 and 4.89×10^4 el/cm^3; these RMSEs are 30%–50% smaller than the IRI-2016 predictions. Besides, the performances of the ANN-TDD in summer and autumn are better than those in spring and winter. This phenomenon is also observed over the Jicamarca ISR, located in a near-equator region. Gowtam et al. (2019) used long-term ionospheric observations from ground-based Digisondes, satellite-based topside sounders and RO measurements to build an ANN-based three-dimensional ionospheric model (ANNIM-3D). In the 0°–30° and 30–60° dip latitudes, the RMSEs of the predicted residuals of ANNIM-3D were 3.9×10^5 and 1.6×10^5 el/cm^3 compared with satellite in situ observations by CHAMP, and the predicted residuals of the ANNIM-3D are larger than the ANN-TDD model. The different predicted capabilities may be associated with the strategies used in developing ANN models. In Gowtam et al.'s study, the globally distributed electron densities derived from multiple missions were divided into 840 small spatial grids, and the vertical profiles in each grid were trained to generate a regional ANN-based model. Unlike Gowtam et al.'s study, in the training stage of the ANN-TDD, the entire multi-source ionospheric profiles are trained to establish an ANN-based ionospheric model using a mini-batch strategy.

Generally, the ANN-TDD model has a weaker predicted capability under severe geomagnetic storms compared to the IRI-2016 with the STORM option activated. At middle latitudes, both of the predicted profiles of the ANN-TDD and IRI-2016 agree well with the measurements obtained from the Millstone Hill ISR at the bottom-side ionosphere, but neither of the two models successfully capture the sharp electron density enhancement at the topside ionosphere. The RMSE and STD of the predicted residuals of the ANN-TDD are worse than those of the IRI-2016. At the near-equator region, the predicted accuracy of the ANN-TDD is also slightly lower than the IRI-2016 at the Jicamarca ISR. However, the prediction stability of the ANN-TDD is significantly superior to the IRI-2016. The weaker predicted capability under severe geomagnetic conditions is believed to be associated with insufficient observations. Compared to the profiles in quiet conditions, the observations under severe geomagnetic conditions are about 5% of the total measurements. In the training process, the disturbed electron density profiles can easily be regarded as "noisy" values. Therefore, the ANN technique has difficultly capturing the nonlinear relationships between ionospheric evolutions and violent space weather parameters. The success of the IRI-2016 indicates to us that it is necessary to develop a STORM option for the ANN-TDD model. The authors will continue to improve the predicted capability for severe space weather in this respect in further studies.

To further validate the ANN-TDD's capability in capturing large-scale ionospheric dynamic characteristics, the RO observations obtained from the FORMOSAT/COSMIC-2 constellation during December 2019 and March 2020 are used to reconstruct global ionosphere electron density maps at altitudes from 200 to 400 km. The ANN-TDD model successfully reproduced the global ionospheric dynamic features and the interhemispheric asymmetries during the winter solstice (Figure 9). Furthermore, some prominent regional ionospheric anomalies are well represented by the ANN-TDD model, such as the EIA, Weddell Sea anomaly, MSNA, etc. The new model successfully captures the vertical structures and diurnal evolution of the EIA, Weddell Sea anomaly and MSNA. The results demonstrate that the ANN-TDD model successfully captures global ionospheric spatial-temporal characteristics and reconstructs the dynamic structures of prominent regional anomalies over the magnetic equator (Figures 8 and 9), middle latitudes (Figure 11) and polar regions (Figure 10), which can play an important role in reducing the ionospheric delay effect and in discovering the physical mechanisms responsible for ionospheric dynamic transportation and convection.

Furthermore, the ANN-TDD model usually underestimates the electron density compared to the RO profiles derived from the COSMIC-1 and COSMIC-2 constellations; this can be seen from the validation results in Figures 7–9. In the retrieval of vertical electron density profiles by the Abel method, the spherical structures are usually assumed to be uniform. However, this assumption is often violated in the low-middle latitude areas, especially around the crests where the horizontal density gradients are larger. Therefore, the systematic errors produced in the retrieval process of the Abel method are also introduced into the ANN-TDD model. (Ram et al., 2016) have proposed a self-contained global ionospheric map (GIM)-aided Abel retrieval method that can account for spherical inhomogeneity. This method is available to retrieve more accurate RO profiles in near real-time. Therefore, an improvement of the retrieval quality of GNSS RO profiles by a new Abel method will be conducted in our further studies.

Finally, the low-latitude equatorial ionization region is the most complex in the world. The variability of the low-latitude ionosphere is controlled by large-scale electrodynamics associated with the equatorial electrojet (EEJ), equatorial winds, temperature anomaly, equatorial ionization anomaly, plasma fountain, etc. However, due to the quantitative limitation of ionospheric observations, it is still a great challenge to fully monitor the ionospheric horizontal-vertical electrodynamic conventions over low latitudes. With the full deployment of the COSMIC-2 constellation, formed from six satellites in different orbital planes, this constellation could provide 4,000+ electron density profiles that are 3–4 times larger than the daily observations of the COSMIC-1 mission over the low latitudes. This large data volume will improve the accuracies of weather forecasts remarkably, and it has been already used to develop a numerical weather prediction model by several major weather organizations around the world. Therefore, the electron density products retrieved from the new COSMIC mission will be utilized to further develop the ANN-TDD model to improve its predicted performance in the complex latitude zone.

Data Availability Statement

The COSMIC data available in UCAR community programs. The Ionosonde data available from the Lowell GIRO Data Center and the solar-magnetic indices available in GSFC.

References

Anderson, D., Buonsanto, M., Codrescu, M., Decker, D., Fesen, C., Fuller-Rowell, T., et al. (1998). Intercomparison of physical models and observations of the ionosphere. *Journal of Geophysical Research*, *103*(A2), 2179–2192.

Athieno, R., Jayachandran, P., & Themens, D. (2017). A neural network-based foF2 model for a single station in the polar cap. *Radio Science*, *52*(6), 784–796.

Atıcı, R., & Sağır, S. (2020). Global investigation of the ionospheric irregularities during the severe geomagnetic storm on September 7–8, 2017. *Geodesy and Geodynamics*, *11*(3), 211–221.

Balan, N. B., & Bailey, G. J. (1995). Equatorial plasma fountain and its effects: Possibility of an additional layer. *Journal of Geophysical Research*, *100*(A11), 21421–21432.

Bellchambers, W., & Piggott, W. (1958). Ionospheric measurements made at Halley Bay. *Nature*, *182*(4649), 1596–1597.

Bilitza, D., & Reinisch, B. W. (2008). International reference ionosphere 2007: Improvements and new parameters. *Advances in Space Research*, *42*(4), 599–609.

Burns, A., Zeng, Z., Wang, W., Lei, J., Solomon, S., Richmond, A., et al. (2008). Behavior of the F2 peak ionosphere over the South Pacific at dusk during quiet summer conditions from COSMIC data. *Journal of Geophysical Research*, *113*(A12). https://doi.org/10.1029/2008JA013308

Chen, C.-H., Saito, A., Lin, C.-H., & Liu, J. (2012). Long-term variations of the nighttime electron density enhancement during the iono-spheric midlatitude summer. *Journal of Geophysical Research*, *117*(A7). https://doi.org/10.1029/2011JA017138

Danilov, A., & Lastovicka, J. (2001). Effects of geomagnetic storms on the ionosphere and atmosphere. *International Journal of Geomag-netism and Aeronomy*, *2*(3), 209–224.

Du, W., Liu, X., Guo, J., Shen, Y., Li, W., & Chang, X. (2019). Analysis of the melting glaciers in Southeast Tibet by ALOS-PALSAR data. *Terrestrial, Atmospheric and Oceanic Sciences*, *30*, 1–13.

Fuller-Rowell, T., Codrescu, M., Moffett, R., & Quegan, S. (1994). Response of the thermosphere and ionosphere to geomagnetic storms. *Journal of Geophysical Research*, *99*(A3), 3893–3914.

Galkin, I. A., & Reinisch, B. W. (2008). The new ARTIST 5 for all digisondes. *Ionosonde Network Advisory Group Bulletin*, *69*(8), 1–8.

Gowtam, V. S., Tulasi Ram, S., Reinisch, B., & Prajapati, A. (2019). A new artificial neural network-based global three-dimensional ion-ospheric model (ANNIM-3D) using long-term ionospheric observations: Preliminary results. *Journal of Geophysical Research: Space Physics*, *124*(6), 4639–4657. https://doi.org/10.1029/2019JA026540

Hajra, R., Tsurutani, B. T., Brum, C. G., & Echer, E. (2017). High-speed solar wind stream effects on the topside ionosphere over Arecibo: A case study during solar minimum. *Geophysical Research Letters*, *44*(15), 7607–7617.

Haykin, S. (2007). *Neural networks*. A Comprehensive FoundationPrentice-Hall, Inc.

He, C., Yang, Y., Carter, B., Zhang, K., Hu, A., Li, W., et al. (2020). Impact of thermospheric mass density on the orbit prediction of LEO satellites. *Space Weather*, *18*(1), e2019SW002336.

Hernandez-Pajares, M., Juan, J., & Sanz, J. (1997). Neural network modeling of the ionospheric electron content at global scale using GPS data. *Radio Science*, *32*(3), 1081–1089.

Horvath, I. (2006). A total electron content space weather study of the nighttime Weddell Sea Anomaly of 1996/1997 southern summer with TOPEX/Poseidon radar altimetry. *Journal of Geophysical Research*, *111*(A12). https://doi.org/10.1029/2006JA011679

Hu, A., & Zhang, K. (2018). Using bidirectional long short-term memory method for the height of F2 peak forecasting from ionosonde measurements in the Australian region. *Remote Sensing*, *10*(10), 1658.

Jin, S., Jin, R., & Kutoglu, H. (2017). Positive and negative ionospheric responses to the March 2015 geomagnetic storm from BDS obser-vations. *Journal of Geodesy*, *91*(6), 613–626.

Karatay, S. (2020). Temporal variations of the ionospheric disturbances due to the seasonal variability over Turkey using IONOLAB-FFT algorithm. *Geodesy and Geodynamics*, *11*(3), 182–191.

Lei, J., Liu, L., Wan, W., Zhang, S.-R., & Van Eyken, A. (2006). Comparison of the first long-duration IS experiment measurements over Millstone Hill and EISCAT Svalbard radar with IRI2001. *Advances in Space Research*, *37*(5), 1102–1107.

Li, W., Yue, J., Guo, J., Yang, Y., Zou, B., Shen, Y., & Zhang, K. (2018). Statistical seismo-ionospheric precursors of M7. 0+ earthquakes in Circum-Pacific seismic belt by GPS TEC measurements. *Advances in Space Research*, *61*(5), 1206–1219.

Li, W., Yue, J., Yang, Y., He, C., Hu, A., & Zhang, K. (2018). Ionospheric and thermospheric responses to the recent strong solar flares on 6 September 2017. *Journal of Geophysical Research: Space Physics*, *123*(10), 8865–8883. https://doi.org/10.1029/2018JA025700

Li, W., Zhao, D., He, C., Hu, A., & Zhang, K. (2020). Advanced machine learning optimized by the genetic algorithm in ionospheric models using long-term multi-instrument observations. *Remote Sensing*, *12*(5), 866.

Li, W., Zhao, D., Shen, Y., & Zhang, K. (2020). Modeling Australian TEC maps using long-term observations of Australian regional GPS network by artificial neural network-aided spherical cap harmonic analysis approach. *Remote Sensing*, *12*(23), 3851.

Liao, M., Zhang, P., Guang-Lin, Y., Yan-Meng, B., Liu, Y., Wei-Hua, B., et al. (2016). Preliminary validation of the refractivity from the new radio occultation sounder GNOS/FY-3C. *Atmospheric Measurement Techniques*, *9*(2), 781.

Lin, C.-H., Liu, C.-H., Liu, J.-Y., Chen, C.-H., Burns, A. G., & Wang, W. (2010). Midlatitude summer nighttime anomaly of the ionospheric electron density observed by FORMOSAT-3/COSMIC. *Journal of Geophysical Research*, *115*(A3). https://doi.org/10.1029/2009JA014084

Lin, C.-H., Liu, J.-Y., Cheng, C.-Z., Chen, C.-H., Liu, C.-H., Wang, W., et al. (2009). Three-dimensional ionospheric electron density struc-ture of the Weddell Sea Anomaly. *Journal of Geophysical Research*, *114*(A2). https://doi.org/10.1029/2008JA013455

Lin, C. H., Wenbin, W., Hagan, M. E., Hsiao, C., Immel, T., Hsu, M., et al. (2007). Plausible effect of atmospheric tides on the equatorial ion-osphere observed by the FORMOSAT-3/COSMIC: Three-dimensional electron density structures. *Geophysical Research Letters*, *34*(11).

Maltseva, O., & Glebova, G. (2020). Comparison of TEC prediction methods in mid-latitudes with GIM maps. *Geodesy and Geodynamics*, *11*(3), 174–181.

Mansilla, G. A. (2019). Behavior of the total electron content over the Arctic and Antarctic sectors during several intense geomagnetic storms. *Geodesy and Geodynamics*, *10*(1), 26–36.

Provost, F., & Kohavi, R. (1998). Glossary of terms. *Journal of Machine Learning*, *30*(2–3), 271–274.

Raghavarao, R., Nageswararao, M., Hanumath Sastri, J., Vyas, G. D., & Sriramarao, M. (1988). Role of equatorial ionization anomaly in the initiation of equatorial spread F. *Journal of Geophysical Research*, *93*(A6), 5959–5964.

Ram, S. T., Su, S.-Y., Tsai, L.-C., & Liu, C. H. (2016). A self-contained GIM-aided Abel retrieval method to improve GNSS-Radio Occultation retrieved electron density profiles. *GPS Solutions*, *20*(4), 825–836.

Richmond, A., Ridley, E., & Roble, R. (1992). A thermosphere/ionosphere general circulation model with coupled electrodynamics. *Geo-physical Research Letters*, *19*(6), 601–604.

Roble, R., & Ridley, E. (1994). A thermosphere-ionosphere-mesosphere-electrodynamics general circulation model (TIME-GCM): Equi-nox solar cycle minimum simulations (30–500 km). *Geophysical Research Letters*, *21*(6), 417–420.

Roble, R., Ridley, E. C., Richmond, A., & Dickinson, R. (1988). A coupled thermosphere/ionosphere general circulation model. *Geophysical Research Letters*, *15*(12), 1325–1328.

Schunk, R., Raitt, W., & Banks, P. (1975). Effect of electric fields on the daytime high-latitude E and F regions. *Journal of Geophysical Research*, *80*(22), 3121–3130.

Schunk, R., & Walker, J. (1973). Theoretical ion densities in the lower ionosphere. *Planetary and Space Science*, *21*(11), 1875–1896.

Sivavaraprasad, G., Deepika, V., SreenivasaRao, D., Kumar, M. R., & Sridhar, M. (2020). Performance evaluation of neural network TEC forecasting models over equatorial low-latitude Indian GNSS station. *Geodesy and Geodynamics*, *11*(3), 192–201.

Thampi, S. V., Lin, C., Liu, H., & Yamamoto, M. (2009). First tomographic observations of the midlatitude summer nighttime anomaly over Japan. *Journal of Geophysical Research*, *114*(A10). https://doi.org/10.1029/2009JA014439

Tsai, Y., Huang, C., Yeh, W., Chen, K., Chen, S., Tseng, T., & Tsai, Y. (2019). *Calibration and validation of FORMOSAT-7/COSMIC-2: TROPS preliminary results*. *AGUFM. 2019*, G21B-0732.

Tulasi Ram, S., Sai Gowtam, V., Mitra, A., & Reinisch, B. (2018). The improved two-dimensional artificial neural network-based ionospher-ic model (ANNIM). *Journal of Geophysical Research: Space Physics*, *123*(7), 5807–5820. https://doi.org/10.1029/2018JA025559

Tulasi Ram, S., Su, S. Y., & Liu, C. (2009). FORMOSAT-3/COSMIC observations of seasonal and longitudinal variations of equatorial ionization anomaly and its interhemispheric asymmetry during the solar minimum period. *Journal of Geophysical Research*, *114*(A6). https://doi.org/10.1029/2008JA013880

Williscroft, L. A., & Poole, A. W. (1996). Neural networks, foF2, sunspot number and magnetic activity. *Geophysical Research Letters*, *23*(24), 3659–3662.

Xiong, C., & Lühr, H. (2014). The Midlatitude Summer Night Anomaly as observed by CHAMP and GRACE: Interpreted as tidal features. *Journal of Geophysical Research: Space Physics*, *119*(6), 4905–4915. https://doi.org/10.1002/2014JA019959